Opto-Electronic Science

Supplementary information

July 2023, Vol. 2, No. 7

DOI: 10.29026/oes.2023.230010

8-nm narrowband photodetection in diamonds

Lemin Jia, Lu Cheng and Wei Zheng*

State Key Laboratory of Optoelectronic Materials and Technologies, School of Materials, Sun Yat-sen University, Shenzhen 518107, China.
*Correspondence: W Zheng, E-mail: zhengw37@mail.sysu.edu.cn

This file includes:

Figures S1 to S9

Supplementary information for this paper is available at https://doi.org/10.29026/oes.2023.230010

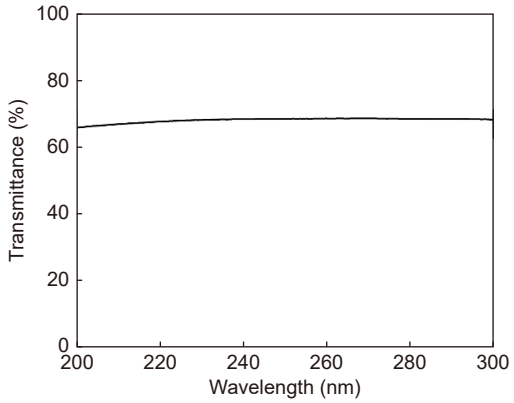

Fig. S1 | Transmittance of the top Pt semitransparent electrode, which is less than 70%. On the MgF_2 substrate sputtered a Pt electrode with the same condition as that of device, and the transmittance of Pt electrode can be obtained by being compared with the transmittance of MgF_2 substrate.

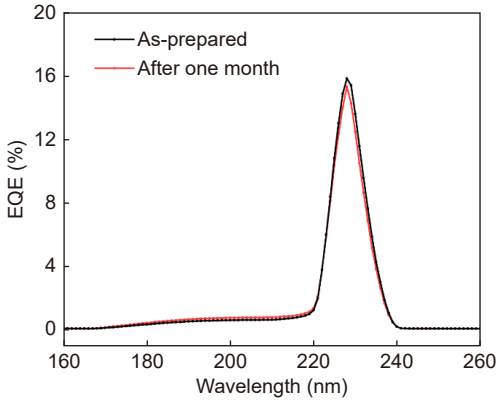

Fig. S2 | EQE spectra of as-prepared diamond A-based photodetector and the same device after one-month storage in the air. There was no significant change in device performance.

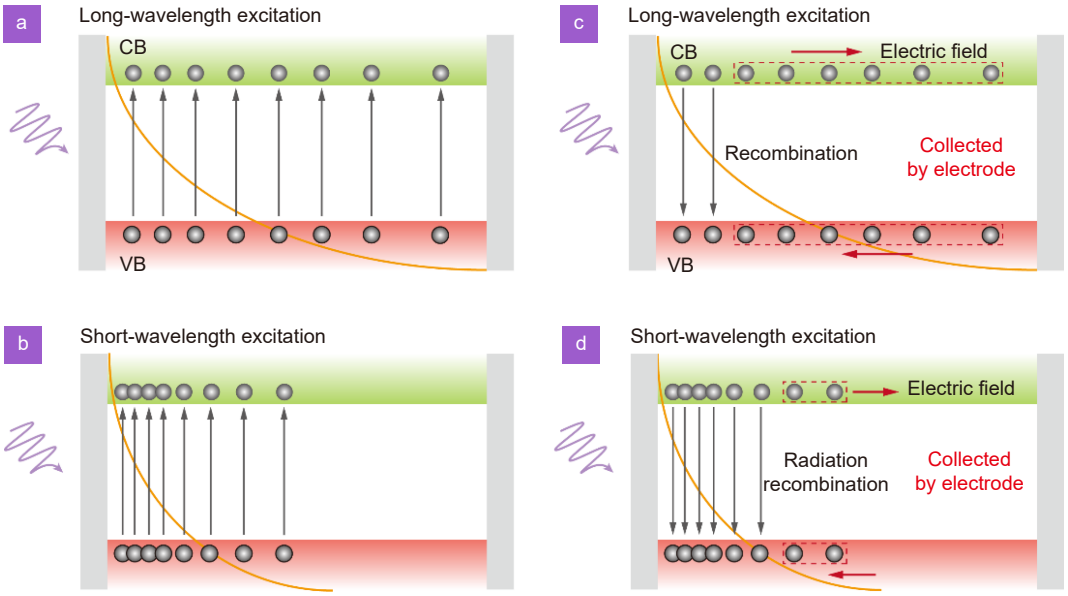

Fig. S3 | Schematic diagram of narrowband photodetection mechanism of diamond A. Under long-wave excitation, photogenerated carriers can be excited within the entire crystal to be collected by electrodes under the action of an electric field. After reaching the peak of response, as excitation wavelength continues to decrease, photogenerated carriers generated will be more and more concentrated on the surface of crystal and annihilated mainly through the radiative recombination process rather than being transmitted to the back of crystal and then get collected by the electrodes. This schematic diagram only aims to give an intuitive image without real physical meaning.

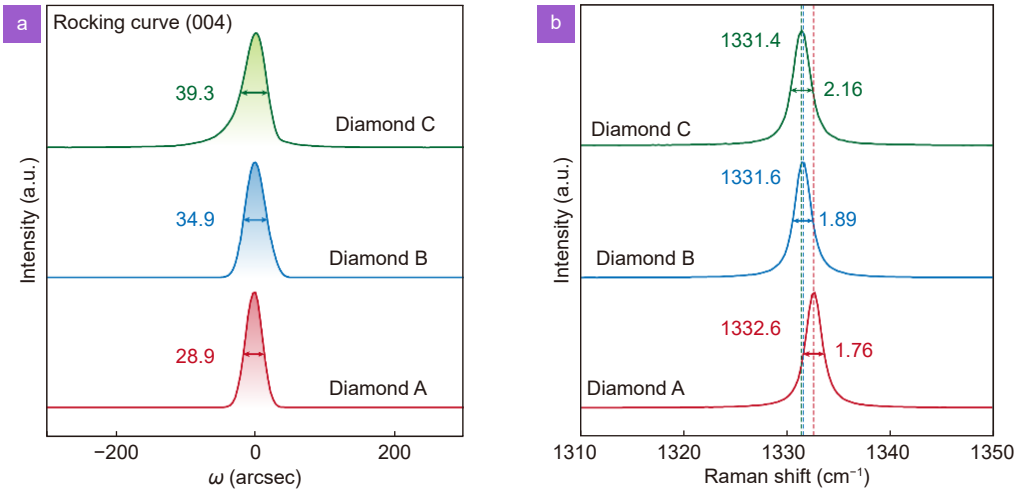

Fig. S4 | X-ray rocking curves and Raman spectra of diamonds. (**a**) X-ray rocking curves of (004) planes of diamonds A, B, and C, with FWHMs as 28.9, 34.9, and 39.3 arcsec, respectively. (**b**) Raman spectra of diamonds A, B, and C.

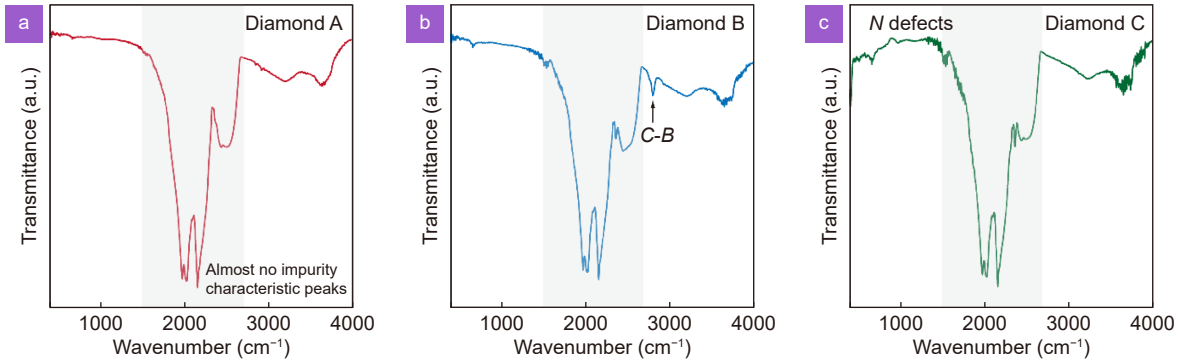

Fig. S5 | Infrared spectra of diamonds A, B, and C. The grey area refers to the characteristic peak region of diamond. Almost no other impurity peaks can be observed in diamond A, different from the situation of diamonds B and C. Diamond B and C are characterized by distinct boron and nitrogen impurities, respectively. This result indicates that diamond A has the highest purity.

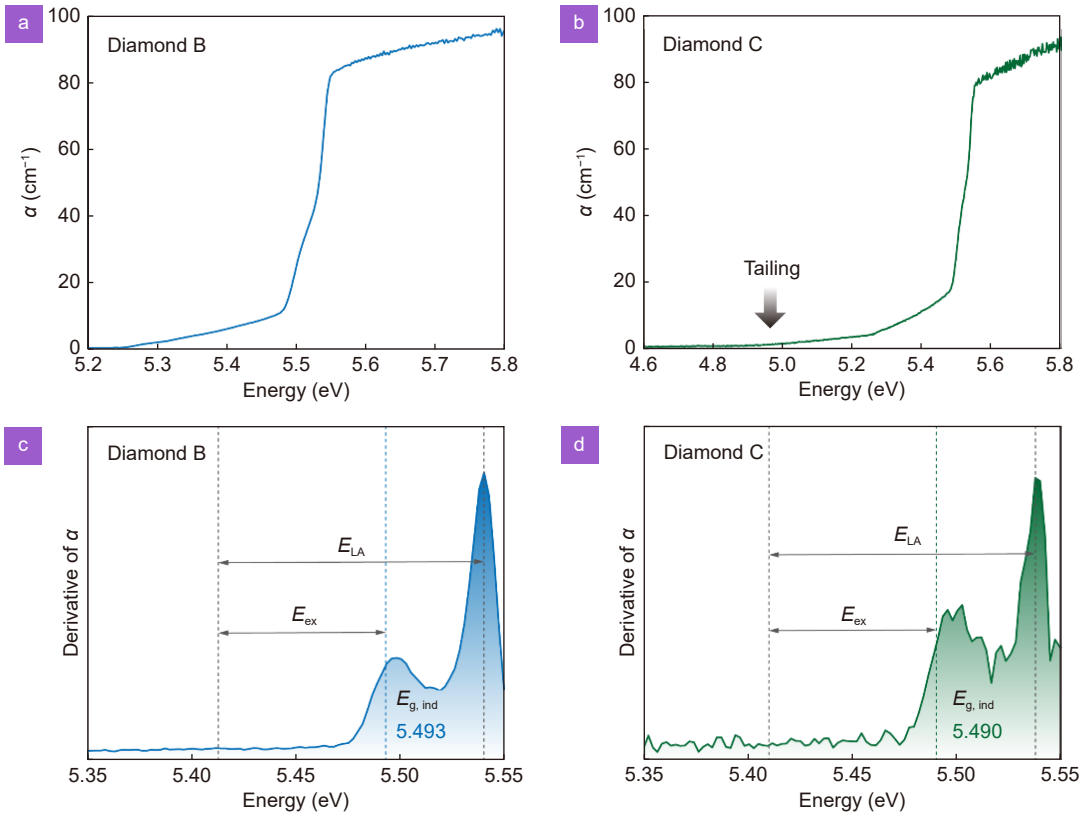

Fig. S6 | Absorption coefficient and differential absorption coefficient spectra of diamonds B and C. (**a**, **b**) Absorption spectra of diamonds B and C. The absorption edge of diamond C exhibits an obvious tailing. (**c**, **d**) Differential spectra of the absorption coefficients of diamonds B and C. Corresponding band gaps can be obtained as 5.493 eV and 5.490 eV, respectively.

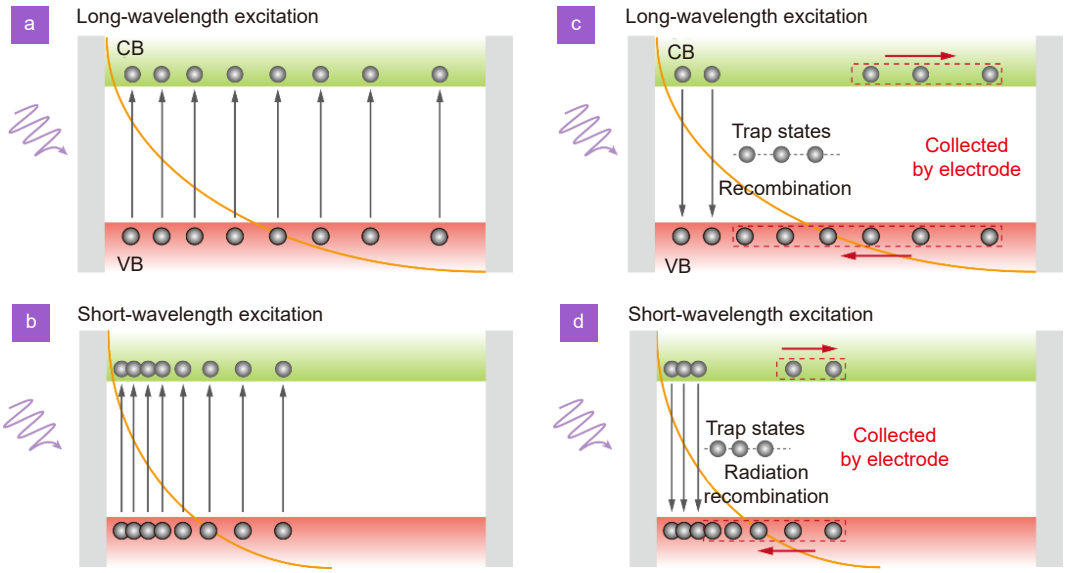

Fig. S7 | Schematic diagram of the broadband photodetection mechanism of diamond C. The high dislocation density owned by diamond C leads to a large number of trap states in the crystal, which brings the carriers trapped a long lifetime. Under an excitation with shorter wavelength light, although carriers generated are close to the surface, they can still diffuse into the crystal interior due to small radiative recombination. At the same time, due to the long carrier lifetime, carriers can be collected by the back electrodes under the action of an electric field, which thus prohibits a decline of photoresponse. This schematic diagram aims to give an intuitive image rather than real physical meanings.

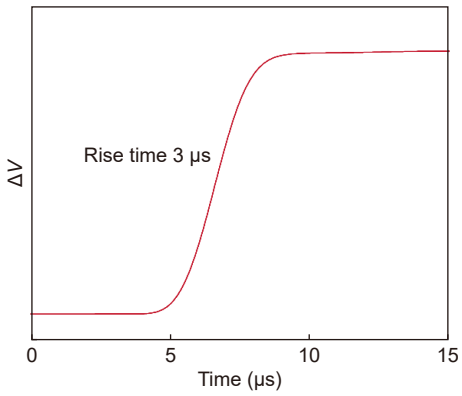

Fig. S8 | Enlarged pulse response image of the device based on Diamond A, indicating a rise time of 3 μs.

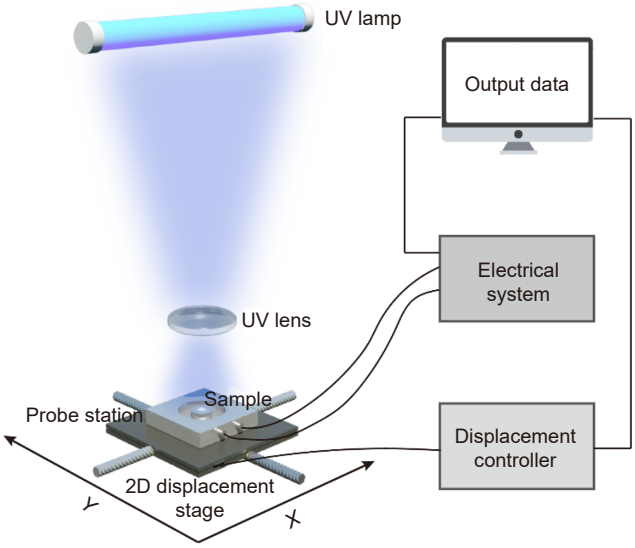

Fig. S9 | Schematic of imaging test of narrowband photodetectors. The UV radiation from a lamp is focused on the plane of that sample through a quartz lenticular lens. The sample is placed on a miniature probe station to obtain electrical signals, which is moved by a two-dimensional stage to achieve image scanning with a displacement step of 500 μm.